Acta Pharmaceutica Sinica B 2025;15(9):4917−4931

Chinese Pharmaceutical Association
Institute of Materia Medica, Chinese Academy of Medical Sciences

Acta Pharmaceutica Sinica B

www.elsevier.com/locate/apsb
www.sciencedirect.com

ORIGINAL ARTICLE

A novel dual-targeting strategy of nanobody-driven protein corona modulation for glioma therapy

Yupei Zhang[a,†], Shugang Qin[b,†], Tingting Song[a,†], Zhiying Huang[a], Zekai Lv[a], Yang Zhao[a], Xiangyu Jiao[a], Min Sun[a], Yinghan Zhang[a], Guang Xie[a], Yuting Chen[a], Xuli Ruan[a], Ruyue Liu[a], Haixing Shi[a], Chunli Yang[a], Siyu Zhao[a], Zhongshan He[a], Hai Huang[a,*], Xiangrong Song[a,*]

[a]*Department of Critical Care Medicine, Frontiers Science Center for Disease-Related Molecular Network, State Key Laboratory of Biotherapy, West China Hospital, Sichuan University, Chengdu 610041, China*
[b]*Department of Experimental Research, Sichuan Clinical Research Center for Cancer, Sichuan Cancer Hospital & Institute, Sichuan Cancer Center, University of Electronic Science and Technology, Chengdu 610040, China*

Received 9 January 2025; received in revised form 21 March 2025; accepted 28 April 2025

KEY WORDS

Glioma;
BBB;
Cisplatin;
Lipid nanoparticles;
Dual-targeting;
Nanobody;
Protein coronas;
Hitchhiking effect

Abstract Glioma represents the most prevalent malignant tumor of the central nervous system, with chemotherapy serving as an essential adjunctive treatment. However, most chemotherapeutic agents exhibit limited ability to penetrate the blood−brain barrier (BBB). This study introduced a novel dual-targeting strategy for glioma therapy by modulating the formation of nanobody-driven protein coronas to enhance the brain and tumor-targeting efficiency of hydrophobic cisplatin prodrug-loaded lipid nanoparticles (C8Pt-Ls). Specifically, nanobodies (Nbs) with fibrinogen-binding capabilities were conjugated to the surface of C8Pt-Ls, resulting in the generation of Nb-C8Pt-Ls. Within the bloodstream, Nb-C8Pt-Ls could bound more fibrinogen, forming the protein corona that specifically interacted with LRP-1, a receptor highly expressed on the BBB. This interaction enabled a "Hitchhiking Effect" mechanism, facilitating efficient *trans*-BBB transport and promoting effective brain targeting. Additionally, the protein corona interacted with LRP-1, which is also overexpressed in glioma cells, achieving precise tumor targeting. Computational simulations and SPR detection clarified the molecular interaction mechanism of the Nb-fibrinogen-(LRP-1) complex, confirming its binding specificity and stability. Our results

*Corresponding authors.
E-mail addresses: songxr@scu.edu.cn (Xiangrong Song), 676055603@qq.com (Hai Huang).
†These authors made equal contributions to this work.
Peer review under the responsibility of Chinese Pharmaceutical Association and Institute of Materia Medica, Chinese Academy of Medical Sciences.

https://doi.org/10.1016/j.apsb.2025.07.014

demonstrated that this strategy significantly enhanced C8Pt accumulation in brain tissues and tumors, induced apoptosis in glioma cells, and improved therapeutic efficacy. This study provides a novel framework for glioma therapy and underscores the potential of protein corona modulation-based dual-targeting strategies in advancing treatments for brain tumors.

1. Introduction

The effectiveness of chemotherapy for gliomas depended on the ability of drugs to cross the blood−brain barrier (BBB) and accumulate in intracranial tumor tissue, a critical yet challenging area in glioma therapy development[1,2], which is a type of primary brain tumor, accounted for approximately 80% of malignant tumors in the central nervous system (CNS), with an annual incidence ranging from 30 to 80 cases per million individuals[3,4]. Certain chemotherapeutic agents, such as temozolomide, the standard treatment for glioma, made incremental progress in overcoming these barriers[5]. However, temozolomide required high dosages, was costly, and was associated with significant side effects and the development of drug resistance[6]. Other conventional chemotherapy drugs, including carmustine, lomustine, irinotecan, cisplatin (CisPt), carboplatin, and cyclophosphamide, were also used in glioma treatment. While these agents were effective against non-intracranial solid tumors, their limited BBB penetration and low intracranial concentrations restricted their clinical utility in glioma therapy[1,7]. Therefore, developing new strategies for efficiently delivering these drugs to the brain and selectively targeting glioma tissue could result in more effective treatments and improved surgical outcomes.

Pt-based drugs, such as CisPt, carboplatin, and oxaliplatin, were first-line treatments for various solid tumors, including lung, ovarian, prostate, and testicular cancers[8]. Approximately 70%−80% of patients with solid tumors received chemotherapy regimens containing Pt-based agents[9]. However, these drugs were primarily considered second-line treatments for gliomas due to their limited ability to cross the BBB and achieve therapeutic concentrations in glioma tissue, thereby reducing their anticancer efficacy compared to other solid tumors[10,11]. Current research on Pt-based drugs and novel delivery methods focused on enhancing tumor selectivity and reducing toxicity to normal tissues[12-16]. Nevertheless, few studies specifically addressed the development of Pt-based drugs and delivery strategies for glioma. The challenge lay not only in improving tumor selectivity but also in enabling these drugs to effectively cross the BBB and target intracranial glioma tissue. Tetravalent Pt prodrugs represented a new class of Pt-based compounds designed to enhance the pharmacological properties of traditional divalent Pt agents. These prodrugs formed a stable octahedral coordination structure and exhibited lower reactivity in bodily fluids compared to divalent Pt-based drugs[17]. Once inside tumor cells, tetravalent Pt prodrugs were reduced to divalent Pt by the higher intracellular concentrations of glutathione (GSH)[18]. Lipid carrier help Pt drugs decrease toxicity, improve bioavailability, realize tumor targeting, and overcome Pt drug resistance[9]. It was hypothesized that hydrophobic modification of the axial ligand in tetravalent Pt complexes[8,15,19] could facilitate their encapsulation within the hydrophobic core of lipid nanoparticles (LNPs).

The development of drug nanocarriers has opened new possibilities for glioma therapy[20]. However, the surface properties of nanoparticles significantly influence their *in vivo* behaviors, primarily due to the formation of protein coronas—layers of biomolecules adsorbed onto the nanoparticle surface[21-24]. Monoclonal antibodies conjugated with modified nanoparticles have been widely used for targeted tissue delivery[25]. Despite their potential, the high cost, time-consuming production processes, and unstable properties of monoclonal antibodies limited their practical clinical application[26]. Nb, also known as variable domains of heavy chain antibody, consists of a single heavy chain variable region (VHH) along with CH2 and CH3 domains. Unlike conventional antibodies, Nb naturally lacks light chains, making them the smallest naturally occurring antibody fragment capable of binding to biomolecules[27]. Nbs offer several advantages, including ease of production and screening, low immunogenicity, and potential as replacements for monoclonal antibodies in various applications[28]. Based on this, we hypothesized that Nb-modified LNPs could provide an innovative strategy for achieving BBB penetration and targeted delivery to brain tumors by modulating the formation of protein coronas.

Some studies suggested that nanoparticles capable of adsorbing apolipoprotein E (ApoE) from plasma could cross the BBB and penetrate brain tumors[29,30] *via* low-density lipoprotein receptor-associated protein-1 (LRP-1)-mediated endocytosis[31]. This research led us to propose that Nbs targeting other plasma proteins, such as fibrinogen[32-34], could similarly regulate protein coronas on LNP surfaces, thereby enhancing BBB penetration and tumor targeting. Based on these insights, we modified hydrophobic CisPt-loaded prodrug liposomes with anti-fibrinogen Nbs. By manipulating protein corona formation on the nanoparticle surface, we aimed to utilize fibrinogen's "Hitchhiking Effect" to facilitate drug penetration across the BBB and enhance glioma tissue targeting.

This study explored the mechanisms by which protein coronas regulate a novel brain-targeted Pt prodrug delivery system for crossing the BBB and targeting brain tumors, while also evaluating its therapeutic efficacy against glioma. The graphical abstract is presented in Fig. 1. Specifically, we employed a microfluidic device to conjugate anti-fibrinogen Nbs to the surface of hydrophobic CisPt prodrug (C8Pt) LNPs, creating Nb-C8Pt-Ls. We then sequenced the protein coronas adsorbed onto the LNP surfaces to determine whether Nb modification altered the composition and quantity of protein coronas. Additionally, we used computer simulations and surface plasmon resonance (SPR) detection to study the interactions between Nbs on LNP surfaces, fibrinogen in plasma, and the LRP-1 receptor on the BBB and tumor cells. Subsequent *in vitro* experiments were conducted to assess the BBB penetration and glioma cell affinity of Nb-C8Pt-Ls. We also investigated the *in vivo* organ distribution of Nb-C8Pt-Ls. Finally, *in vivo* experiments compared the

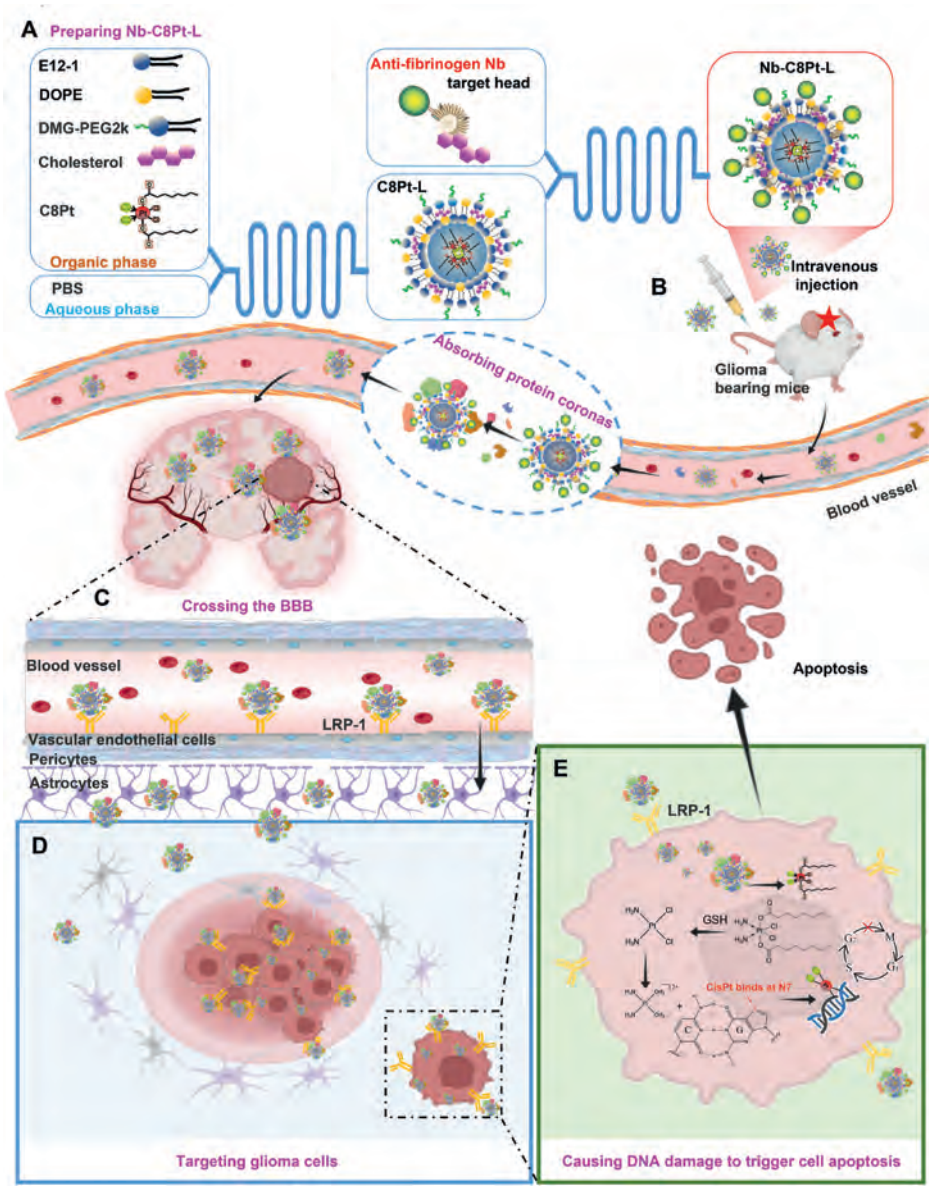

Figure 1 Graphical abstract of Nb-C8Pt-Ls protecting against brain glioma. (A) Preparation of Nb-C8Pt-Ls: C8Pt-Ls (C8Pt LNPs) were prepared by microfluidic mixing of an aqueous phase with an organic phase containing E12-1, DOPE, DMG-PEG2K, cholesterol, and C8Pt (CisPt modified with two 8-carbon side chains). Nb-C8Pt-Ls (anti-fibrinogen Nb-decorated C8Pt LNPs) were created through a second round of microfluidic mixing, where anti-fibrinogen nanobodies (Nbs) were attached to the C8Pt-Ls. (B) Protein corona absorption: once in circulation, the Nb-C8Pt-Ls absorbed protein coronas from plasma, with a particular affinity for fibrinogen, influenced by the anti-fibrinogen Nb modification. (C) BBB penetration: the modification of the LNP surface by protein coronas, especially fibrinogen adsorption, enhanced recognition by LRP-1 on the BBB. This facilitated the nanoparticles' penetration through the BBB after tail vein injection. (D) Targeting glioma cells: due to the fibrinogen-enriched protein coronas on Nb-C8Pt-Ls, these nanoparticles were better recognized by glioma cells, which express high levels of LRP-1, allowing them to specifically target and enter glioma cells in the brain. (E) Inducing DNA damage and apoptosis: once inside glioma cells, Nb-C8Pt-Ls underwent lysosomal escape and release C8Pt. In the intracellular environment with low chloride ion concentrations, C8Pt was reduced by glutathione (GSH) to CisPt, which was transformed into cationic platinum (Pt) hydrates (*Cis*-$[Pt(NH_3)_2(OH_2)_2]^{2+}$). These Pt hydrates crosslinked adjacent DNA bases, leading to DNA damage, arresting the glioma cell cycle at the S/G2 phase, and ultimately triggering apoptosis.

therapeutic efficacy and safety of Nb-C8Pt-Ls with unmodified C8Pt-Ls and CisPt solution in glioma models. Our findings demonstrated that modifying lipid nanoparticles (LNPs) with nanobodies to drive protein corona formation effectively enhanced both brain and tumor targeting. This strategy enabled specific binding to low-density lipoprotein receptor-related protein 1 (LRP-1), which is highly expressed on the BBB and glioma cells. Utilizing a "Hitchhiking Effect" mechanism, the LNPs successfully crossed the BBB, localized to tumor sites, induced apoptosis in glioma cells, and significantly improved therapeutic outcomes. This study establishes a novel framework for glioma therapy and underscores the broad potential of protein corona modulation-based dual-targeting strategies for advancing treatments of brain tumors.

2. Materials and methods

2.1. Synthesis of the CisPt prodrug

A total of 300 mg of CisPt (Sigma−Aldrich: 232120) was suspended in 40 mL of 30% hydrogen peroxide (H_2O_2) and heated at 60 °C for 4 h. After the reaction was completed, the solvent was removed *via* rotary evaporation, and the resulting precipitate was washed with cold ether. The intermediate product, *cis*-$[PtCl_2(NH_3)_2(OH)_2]$, was obtained through freeze-drying. This intermediate was then dispersed in anhydrous dimethylformamide (DMF), and 4 equivalents of octanoic anhydride were added. The reaction was allowed to proceed at 60 °C for 24 h. Upon completion, the solvent was again removed by rotary evaporation, and the target compound, Pt oleate, was purified using a silica gel column.

2.2. Preparation and characterization of C8Pt-Ls and Nb-C8Pt-Ls

The anti-fibrinogen Nb sequence was derived from prior research[35]: MAQVQLVESGGGSVQAGGSLRLSCAASGYTY NNNCMGWFRQAPGKEREGVAVINRGGGRTYYTDSVKGRF TISQDNANNTVYLTMNSLKPEDTAIYYCAARWGWASSSNW YDMGKYNYWGQGTQVTVSS. A GGGGSGGGGS linker and a cysteine residue were added sequentially to the C-terminus of the Nb. After protein synthesis, standard recombinant protein purification techniques were used to purify the Nb. The anti-fibrinogen Nb-targeting moiety was formed by conjugating maleimide-PEG-cholesterol (Mal-PEG-Chol) to the anti-fibrinogen Nb *via* a click reaction.

C8Pt-Ls and Nb-C8Pt-Ls were synthesized using a microfluidic device (Micro&Nano Biologics). The organic phase, consisting of E12-1 lipid (NMR spectra shown in Supporting Information Fig. S1), 1,2-dioleoylphosphatidylethanolamine (DOPE), cholesterol, DMG-PEG2k, and C8Pt, was prepared by ultrasonic dissolution in ethanol at a molar ratio of 35:16:46.5:2.5:15.3. Phosphate-buffered saline (PBS) served as the aqueous phase. To generate C8Pt-Ls, the organic and aqueous phases were mixed within a microfluidic device (INano L, Micro&Nano) at a volume ratio of 1:3 (*v*/*v*), respectively, with a total flow rate of 12 mL/min. Nb-C8Pt-Ls were then prepared by mixing C8Pt-Ls with the anti-fibrinogen Nb-targeting moiety (2.5 μg/μL) at a volume ratio of 1:2 (*v*/*v*), respectively, while maintaining the same flow rate of 12 mL/min. Subsequently, the C8Pt-Ls were diluted with an equal volume of PBS, then ethanol and unbound Nbs were removed *via* ultrafiltration.

The particle size and zeta potential of C8Pt-Ls and Nb-C8Pt-Ls were determined using a Zetasizer Nano ZS90 (Malvern). The morphology of C8Pt-Ls and Nb-C8Pt-Ls was examined using a transmission electron microscope (TEM, H-600, Hitachi).

C8Pt-Ls and Nb-C8Pt-Ls before ultrafiltration were placed in a 100 kDa ultrafiltration tube and centrifuged at 2400×*g* for 15 min. The filtrate (W_{free}) was collected and analyzed *via* inductively coupled plasma mass spectrometry (ICP-MS 7800, Agilent). W_{total} was total Pt adding into the preparation. Encapsulation efficiency of Pt was calculated using Eq. (1):

$$\text{Encapsulation efficiency}\ (\%) = \left(W_{total} - W_{free}\right) / W_{total} \times 100\% \quad (1)$$

To determine the coupling efficiency of anti-fibrinogen Nb, Nb-C8Pt-Ls (prior to ultrafiltration) were placed in a 100 kDa ultrafiltration tube and centrifuged at 2400×*g* for 15 min. The filtrate, containing unbound Nb (W_{free}), was collected and analyzed using a BCA assay (Beyotime, Shanghai, China). W_{total} represented the total anti-fibrinogen Nb added during preparation. Coupling efficiency was calculated using Eq. (2):

$$\text{Coupling efficiency}\ (\%) = \left(W_{total} - W_{free}\right) / W_{total} \times 100\% \quad (2)$$

The stability of the formulation was assessed by measuring the Nb content in the filtrate after storage at 4 °C for 3, 6, and 9 days, and the coupling efficiency was then determined.

To assess fibrinogen adsorption, C8Pt-Ls or Nb-C8Pt-Ls containing 5 μg Pt (0.25 μg/μL) were co-incubated with mouse plasma at a ratio of 1:10 (*v*/*v*) on a shaker. Samples were collected at 0, 5, 10, 20, 30, 60, 120, and 180 min, and precipitation was induced by centrifugation at 13,800×*g*. The precipitate was then treated with RIPA lysis buffer, followed by another centrifugation step. The fibrinogen content in the resulting supernatant was then quantified using a Mouse Fibrinogen (Fbg) ELISA Kit (Jianglai Biology, Shanghai, Cat#JL20600-96T, China), and fibrinogen adsorption curves for the LNPs were generated.

To assess Pt release, C8Pt-Ls or Nb-C8Pt-Ls were placed in a dialysis bag (100 kD) containing PBS (pH 5.5), and the dialysis bag was then immersed in a beaker filled with PBS. At 0, 1, 3, 6, 9, 12, and 15 h, aliquots of the external PBS solution were collected, and the Pt content was quantified by inductively coupled plasma mass spectrometry (ICP-MS, Agilent 7800). A Pt release rate curve was then plotted. The ICP-MS parameters were as follows: pump rate, 20 rpm; nebulizer flow rate, 1 L/min; auxiliary gas flow rate, 1 L/min; sample flush time, 40 s; and RF power, 1550 W.

2.3. Computer simulation of protein molecular docking and surface plasmon resonance

The sequence for the extracellular domain (amino acids 20−4419) of LRP-1 was retrieved from the UNIPROT database (ID: Q07954). AlphaFold 3 (PyMOL Molecular Graphics System, Version 3.0, Schrödinger, LLC) was used to predict the three-dimensional structures of the anti-fibrinogen Nb and LRP-1[36]. The predicted structures of the anti-fibrinogen Nb and LRP-1 are shown in Supporting Information Fig. S2A and S2C, respectively. The crystal structure of fibrinogen was acquired from the RCSB PDB database (ID: 3GHG, Fig. S2B)[37]. Preprocessing of the fibrinogen structure, including the removal of heteroatoms such as solvents and small molecules, was completed using PyMOL. Molecular docking was performed using the HDOCK server. First, the anti-fibrinogen Nb was docked with fibrinogen to generate a set of potential conformations. The optimal conformation of this complex was selected and then docked with LRP-1, resulting in the docking complex of the anti-fibrinogen Nb, fibrinogen, and LRP-1. The most favorable conformation was chosen for further analysis[38-42].

The surface plasmon resonance (SPR)-based binding assays were conducted at 25 ± 2 °C utilizing a BIAcore 1K biosensor platform (Cytiva) with CM5 sensor arrays, where kinetic parameters were determined through multi-channel signal processing and Langmuirian model fitting. Sensor surfaces were covalently modified by sequential perfusion of a coupling cocktail containing

200 μmol/L EDC (1-ethyl-3-(3-dimethylaminopropyl) carbodiimide) and 50 μmol/L NHS (*N*-hydroxysuccinimide) at 10 μL/min for 7 min to generate reactive thiol groups. Recombinant target proteins (50 μL total volume in 10 mmol/L sodium acetate buffer, pH 5.0) were immobilized *via* two consecutive 7-min injections under identical flow conditions. Residual reactive sites were systematically inactivated using 1 mol/L ethanolamine hydrochloride at 10 μL/min for 7 min. A parallel reference channel underwent analogous surface treatment, albeit employing PBS (pH 5.0)-based immobilization to establish baseline signal subtraction. Analyte solutions spanning 5−500 nmol/L concentrations in PBS were introduced at 10 μL/min for 2.5 min per injection cycle, interspersed with 5-min sensor regeneration phases using 10 mmol/L glycine−HCl (pH 2.0). Double-channel subtracted sensorgrams were globally analyzed through nonlinear regression fitting to a 1:1 binding model, yielding association (k_{on}) and dissociation (k_{off}) rate constants with 95% confidence intervals. Final kinetic fingerprints including affinity constants (K_d) were visualized through OriginPro 7.0552 (OriginLab) by generating saturation isotherms and differential binding plots, with all data processed through BIAcore Analysis Suite v2.0 (Cytiva) incorporating reference signal correction.

2.4. Protein corona sequencing

Mouse plasma was centrifuged at 13,000×*g* at 4 °C to remove protein aggregates before use. C8Pt-Ls and Nb-C8Pt-Ls, matched by volume and Pt content, were incubated with an equal volume of C57BL/6J mouse plasma to simulate *in vivo* protein conditions. The samples were incubated at 37 °C for 1 h with constant shaking[43]. After incubation, the protein corona-coated LNPs were isolated by centrifugation at 13,000×*g* for 30 min, followed by three washes with cold PBS to eliminate unbound proteins. Each sample was then treated with an appropriate volume of SDT lysis buffer and heated in boiling water for 5 min. The samples were centrifuged at 15,000×*g* for 20 min at 4 °C, and the supernatant was collected for total protein quantification using a BCA assay (Beyotime, Shanghai, China). The isolated protein coronas were subsequently reduced, alkylated, and digested for mass spectrometry analysis, following procedures outlined in previous studies[44].

2.5. Transwell and cellular uptake experiment

BEnd.3 cells (IMMOCELL, Xiamen, China) were seeded on polycarbonate membranes in the upper chambers of 24-well Transwell plates at a density of 1×10^5 cells per well. The cells were cultured for approximately 20 days. When the transcellular resistance, measured with an epithelial volt-ohmmeter, stabilized at around 200 Ω cm^2 without further increase, it indicated the formation of a tight monolayer, confirming the successful differentiation and establishment of an *in vitro* BBB. At this point, the system was used for Transwell permeability experiments. CisPt, Nb-C8Pt-Ls, and C8Pt-Ls, matched by volume and Pt content (0.25 μg/μL), were pre-incubated with mouse plasma at 37 °C for 1 h with continuous shaking on a shaker. The volume ratio of preparation to plasma was 1:10. Subsequently, the mixtures were added to the upper chamber at a final concentration of 0.5 μg Pt/well. Culture medium from the lower chamber was collected at 0.5, 4, 8, 12, and 24 h. The samples were digested with nitric acid using a microwave digestion system, and Pt content was quantified using inductively coupled plasma mass spectrometry (ICP-MS, Agilent 7800).

Nb-C8Pt-Ls and C8Pt-Ls underwent the same procedure as described above and were subsequently added to the upper chamber at a final concentration of 5 μg Pt/well. Following centrifugation at 13,800×*g*, the supernatant was removed, and the precipitate was collected. After treatment with RIPA buffer, the supernatant was recovered, and its fibrinogen content was quantified using a Mouse Fibrinogen (Fbg) ELISA Kit (Jianglai Biology, Shanghai, Cat#JL20600-96T, China). This measurement represented the fibrinogen carried by the LNPs penetrating the Transwell. The integrity of the fibrinogen coronas on Nb-C8Pt-Ls after Transwell penetration was assessed by comparing it to that of the original preparations.

In a separate experiment, Nb-C8Pt-Ls and C8Pt-Ls underwent the same initial procedure and were subsequently added to the upper chamber at a final concentration of 0.5 μg Pt/well. For the inhibitor treatment group, bEnd.3 cells on the Transwell were pretreated with 50 μmol/L Atorvastatin (LRP-1 inhibitor) for 12 h before the addition of Nb-C8Pt-Ls and C8Pt-Ls. In total, four experimental groups were tested. After 24 h of treatment, the culture medium from the lower chamber of the Transwell was collected and analyzed by ICP-MS. This inhibitor experiment was performed to evaluate the role of LRP-1 in Nb-C8Pt-Ls permeation of bEnd.3 cells.

GL261-LUC (IMMOCELL) and bEnd.3 cells were seeded in 24-well plates at a density of 2×10^5 cells per well and cultured for 12 h. CisPt, Nb-C8Pt-Ls, and C8Pt-Ls were added at a concentration of 0.5 μg Pt/well. After 6 h of incubation, the cells were lysed with RIPA buffer for total protein quantification using a BCA kit, and the Pt content was measured *via* ICP-MS (Agilent 7800).

2.6. Animal treatment

Male C57BL/6J mice, weighing 20−22 g, were purchased from SPF Biotechnology Co., Ltd. (Beijing, China) and housed under controlled circadian rhythm conditions with free access to food and water. The experimental protocol was approved by the Experimental Animal Ethics Committee of West China Hospital. To induce intracranial tumors, GL261-LUC cells were harvested and prepared for implantation. Mice were anesthetized with an intraperitoneal injection of pentobarbital (50 mg/kg) and secured in a stereotactic frame. After disinfecting the dorsal scalp with 70% ethanol, a small incision was made, and a burr hole was drilled into the right striatum (1.9 mm lateral to the sagittal suture and 1.2 mm anterior to the bregma). GL261-LUC cells (1×10^5 cells/10 μL) were injected into the brain at a depth of 3 mm using a microsyringe. The needle was left in place for 5 min before being carefully withdrawn. The burr hole was sealed with bone wax, and the scalp was sutured[45,46]. Glioma-bearing mice were subsequently prepared for the *in vivo* experiments.

2.7. Distribution of lipophilic dye-stained preparations

Lipophilic dyes, DID (AAT Bioquest) and Nile Red (Aladdin), were dissolved in the organic phase using ultrasonic methods. The molar ratios of E12-1 lipid, DOPE, cholesterol (Chol), DMG-PEG2k, C8Pt, and the lipophilic dye were maintained at 35:16:46.5:2.5:15.3:1.4. Lipophilic dye-stained C8Pt-Ls and Nb-C8Pt-Ls were then prepared using the previously described method. Glioma-bearing mice were randomly assigned to 2

groups, with each group receiving a tail vein injection of either stained C8Pt-Ls or Nb-C8Pt-Ls, containing 20 μg of DID. A control group received an equivalent volume of PBS (normal control, NC). Four hours after injection, the mice were anesthetized with isoflurane to take fluorescent photos using the IVIS Lumina III imaging system (PerkinElmer), and their brains were harvested for fluorescent photos *ex vivo*. The same procedure was applied for the Nile Red-stained samples. Tumor-bearing brain tissues from DID-injected mice were sectioned and cryopreserved, followed by DAPI staining of the nuclei. Tumor penetration by DID was sliced, stained nuclei with DAPI, and visualized using confocal laser scanning microscopy (CLSM).

2.8. Distribution of Pt in different organs of glioma-bearing mice

Glioma-bearing mice received intravenous injections of CisPt, C8Pt-Ls, or Nb-C8Pt-Ls, each containing a dose of 20 μg Pt. At 0.5, 4, 8, 12, 24, 48 and 144 h post-injection, samples of the brain, brain tumor, heart, liver, spleen, lungs, kidneys, and plasma were collected. These samples were digested in nitric acid using microwave digestion, and Pt content was measured using ICP-MS (Agilent 7800).

2.9. Anti-brain glioma effects in vivo

The day of glioma cell inoculation was designated as Day 0. Glioma-bearing mice were randomly divided into four groups: Model, CisPt, C8Pt-L, and Nb-C8Pt-L. Starting on Day 6 and continuing until Day 18, the mice in the CisPt, C8Pt-L, and Nb-C8Pt-L groups were intravenously administered 20 μg Pt every 2 days. Body weight and GL261-LUC fluorescence signals were monitored every two days, and survival time was recorded. For GL261-LUC fluorescence imaging, each mouse received an intraperitoneal injection of 150 mg/kg D-luciferin potassium salt (Yeasen, Cat: 40902ES03, Shanghai, China), and imaging was conducted using the IVIS Lumina III system (PerkinElmer). When the mice in the model group reached the terminal stage, all mice were sacrificed. Tumor size was visually inspected on Day 20 using MRI (BioSpec70/30 USR, Bruker), operating at a magnetic field strength of 7T and a gradient field of 300 mT/m. Tissue samples were collected for subsequent pathological and biochemical analysis.

2.10. Immunohistochemical and TUNEL staining

Harvested brain tissues were washed, dried, fixed in 4% paraformaldehyde, and embedded in paraffin before being sectioned into thin slices. Tumor-containing sections were stained with markers for Ki67 (1:200, Abcam, Cat#1ab16667, UK) and cleaved-caspase-3 (1:500, Servicebio, Cat#1GB11532, Wuhan, China). The stained tissues were visualized using a digital microscope (Olympus). Apoptosis in tumor tissues was validated using the TUNEL Apoptosis Detection Kit (Beyotime, Cat#1C1090, Shanghai, China), following the manufacturer's instructions, and images were captured with a fluorescence microscope.

2.11. Western blotting

Tumor tissues were carefully excised from brain samples, and protein expression levels were analyzed by Western blotting. Primary antibodies used in this analysis included anti-γ-H2A.X (1:1000, Bioss, Cat#152163R, Beijing, China), anti-*β*-Catenin (1:1000, ZENBIO, Cat#1R23616, Chengdu, Chian), and anti-GAPDH (1:2000, HUABIO, Cat#1EM1101, Hangzhou, China). The Western blotting procedure followed a standard protocol as described previously[47].

2.12. Blood biochemical analysis, antibody titer detection, coagulation function testing, and HE staining

The safety of the treatments was evaluated by conducting blood biochemical analyses on serum samples collected at the end of the experiment. Key biochemical markers, including albumin (ALB), lactate dehydrogenase (LDH), creatinine (CRE), urea (UREA), creatine kinase-MB (CKMB), alkaline phosphatase (ALP), alanine transaminase (ALT), and aspartate transaminase (AST), were measured using an automatic hematological biochemical analyzer (Hitachi).

The binding titers of the serum samples were quantified using an ELISA platform. Corning high-binding polystyrene microtiter plates were sensitized with anti-Fibrinogen Nbs at a coating concentration of 1 μg/mL. After overnight incubation at 4 °C, the plates were rigorously washed four times with PBS-Tween 20 buffer and then blocked with 2% bovine serum albumin (BSA) in PBS for 4 h at 25 °C. Following the blocking step, the plates were sequentially treated with heat-inactivated (56 °C/30 min) serum samples. Beginning with an initial 1:20 dilution, serial two-fold dilutions were prepared and incubated overnight at 4 °C. After incubation, the plates were washed again four times and then incubated with horseradish peroxidase (HRP)-labeled goat anti-mouse IgG secondary antibody (1:50,000 dilution; Cell Signaling Technology, USA) for 2 h at room temperature. The chromogenic signal was developed using 3,3′-5,5′-tetramethylbenzidine (TMB) substrate (Solarbio, Beijing, China), and the reaction was quenched after 30 min with 2 mol/L sulfuric acid. Optical density was measured at 450 nm using a PerkinElmer microplate spectrophotometer. Endpoint titers were defined as the serum dilution at which the signal exceeded control values.

Plasma was collected from mice at the conclusion of the experiment and thoroughly mixed with two volumes of Prothrombin time (PT) reagent (Shanghai Yaji Biotechnology Co., Ltd.). Following incubation at 37 °C, the reaction was initiated by gently tapping the tube wall, and the time to complete coagulation was recorded.

Additionally, organ samples from the brain, heart, liver, spleen, lungs, and kidneys were processed for hematoxylin and eosin (HE) staining and examined microscopically to assess histological changes.

2.13. Statistical analysis

Quantitative data are analyzed using one-way ANOVA, with a significance threshold of $P < 0.05$. All statistical analyses were performed using SPSS software (version 26.0).

3. Results

3.1. Preparation and characterization of Nb-C8Pt-Ls

The C8Pt prodrug was first synthesized chemically using the method outlined in Fig. 2A, with the corresponding NMR

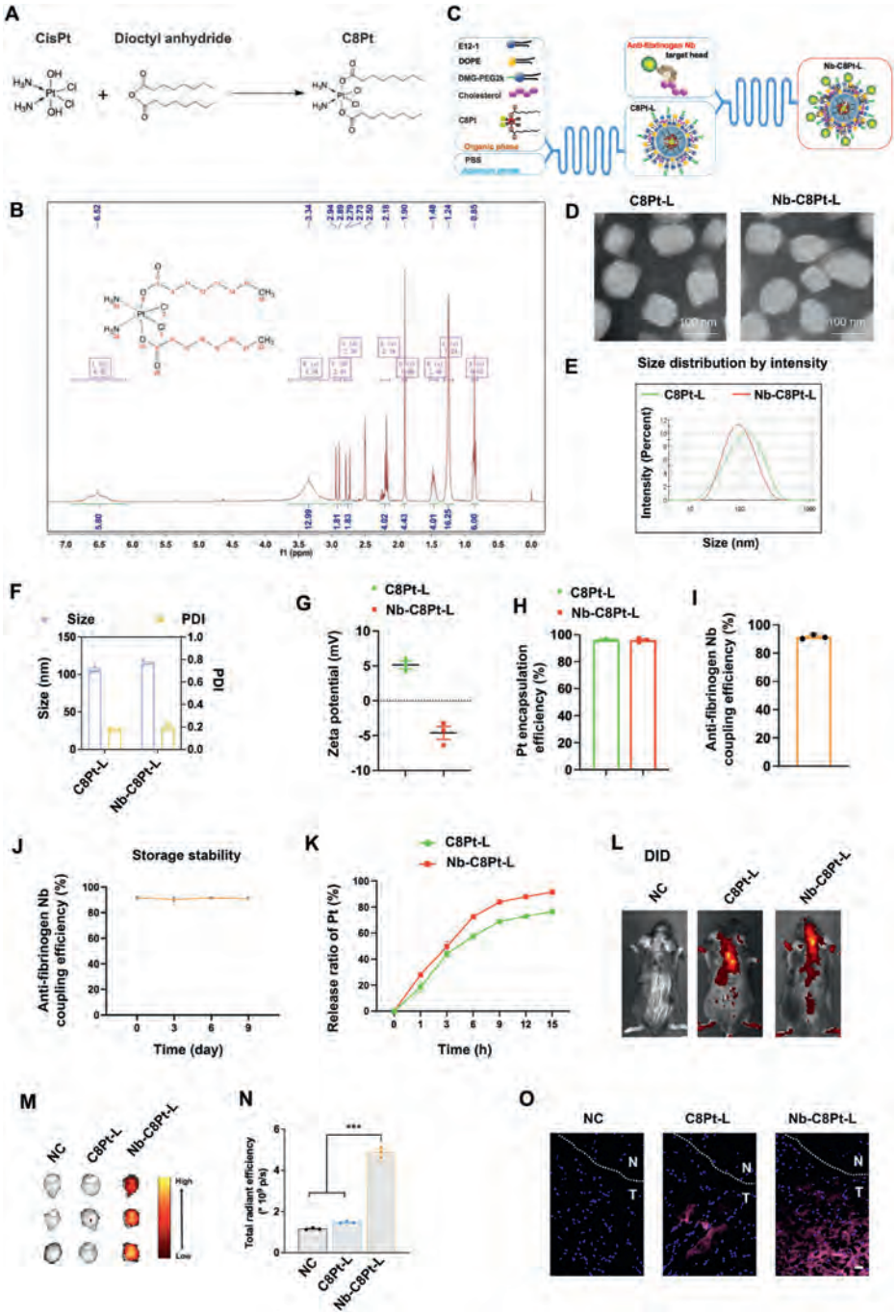

Figure 2 Preparation and characterization of Nb-C8Pt-Ls. (A, B) The chemical synthesis and nuclear magnetic resonance (NMR) spectra of C8Pt, illustrating the synthesis process of C8Pt, a hydrophobically modified CisPt compound with 8-carbon side chains. (C) Schematic representation of nanoparticle preparation using a two-step microfluidic method. The first step prepared C8Pt-Ls (C8Pt LNPs), while the second step decorated these nanoparticles with anti-fibrinogen Nbs, yielding Nb-C8Pt-Ls. (D) Transmission electron microscopy (TEM) images showed the morphology and structure of both C8Pt-Ls and Nb-C8Pt-Ls. (E) Size distribution profiles of C8Pt-Ls and Nb-C8Pt-Ls, indicated the particle size ranges of the formulations. (F) Measurements of particle size and polydispersity index (PDI) for C8Pt-Ls and Nb-C8Pt-Ls, providing insight into nanoparticle uniformity and dispersion. (G) Zeta potential values for C8Pt-Ls and Nb-C8Pt-Ls, indicating the surface charge and stability of the nanoparticles in suspension. (H) Encapsulation efficiency of C8Pt in C8Pt-Ls and Nb-C8Pt-Ls, quantifying the percentage of C8Pt successfully encapsulated in the nanoparticles. (I) Anti-fibrinogen Nb coupling efficiency in Nb-C8Pt-Ls. (J) Storage stability assessment of anti-fibrinogen Nb coupling efficiency in a series of time. (K) Release ratio of Pt with a series of time points. (L, M) Representative images and (N) quantitative analysis of brain-targeting effects for C8Pt-Ls and Nb-C8Pt-Ls loaded with the lipid dye DID in tumor-bearing mice, showing enhanced brain targeting by Nb-C8Pt-Ls compared to C8Pt-Ls at 4 h post-injection. (O) *Ex vivo* confocal laser scanning microscopy (CLSM) images from brain tissues collected in panel (M), demonstrating tumor penetration of DID-loaded Nb-C8Pt-Ls. The nuclei were stained with DAPI (blue), and tumor-penetrating DID fluorescence was shown in red. Tumor and non-tumor regions were labeled as T and N, respectively. Scale bar = 20 μm. Data are presented as mean ± SEM, $n = 3$, with statistical significance indicated by $^{***}P < 0.001$.

spectrum displayed in Fig. 2B. After isolating the anti-fibrinogen nanobodies (Nbs), a two-step microfluidic technique was employed to produce Nb-C8Pt-Ls. Initially, C8Pt-Ls were prepared through the first microfluidic process, followed by a second step in which C8Pt-Ls were conjugated with anti-fibrinogen Nbs, resulting in the formation of Nb-C8Pt-Ls (Fig. 2C). Transmission electron microscopy (TEM) images showed that Nb modification did not alter the shape of the Nb-C8Pt-Ls (Fig. 2D). The particle sizes of C8Pt-Ls and Nb-C8Pt-Ls were measured at 105.67 nm and 115.33 nm, respectively, with polydispersity indices (PDI) of 0.17 and 0.20, and zeta potentials of 5.13 mV and -4.62 mV, respectively (Fig. 2E−G). Encapsulation efficiency was determined to be 83.47% for C8Pt-Ls and 82.95% for Nb-C8Pt-Ls, indicating favorable characteristics for drug delivery (Fig. 2H). The Nb coupling efficiency of Nb-C8Pt-Ls was determined to be 91.47% and remained nearly constant over a storage period of 9 days (Fig. 2I and J). Fig. 2K illustrates that complete release of Pt from both C8Pt-Ls and Nb-C8Pt-Ls occurred within 15 h under acidic conditions (pH = 5.5). To evaluate brain and tumor-targeting capabilities, lipid dyes were incorporated into the Nb-C8Pt-Ls system. Following intravenous injection, Nb-C8Pt-Ls demonstrated more efficient delivery of the dyes DID and Nile Red to the brain compared to C8Pt-Ls alone (Fig. 2L−N and Supporting Information Fig. S3). Fluorescence microscopy further revealed that Nb-C8Pt-Ls facilitated superior delivery of DID to glioma tissue relative to C8Pt-Ls (Fig. 2O). Overall, Nb-C8Pt-Ls exhibited excellent pharmaceutical properties and showed enhanced targeting of both the brain and glioma tissue.

3.2. *Anti-fibrinogen Nb decoration regulated protein corona formation on C8Pt-Ls*

To investigate the impact of anti-fibrinogen Nb decoration on protein corona formation, we analyzed the protein coronas adsorbed by both C8Pt-Ls and Nb-C8Pt-Ls. High-performance liquid chromatography-mass spectrometry (HPLC−MS) revealed subtle differences in the composition of the protein coronas. The proportion of total protein corona abundance within different protein size segments showed only minor variations, with the

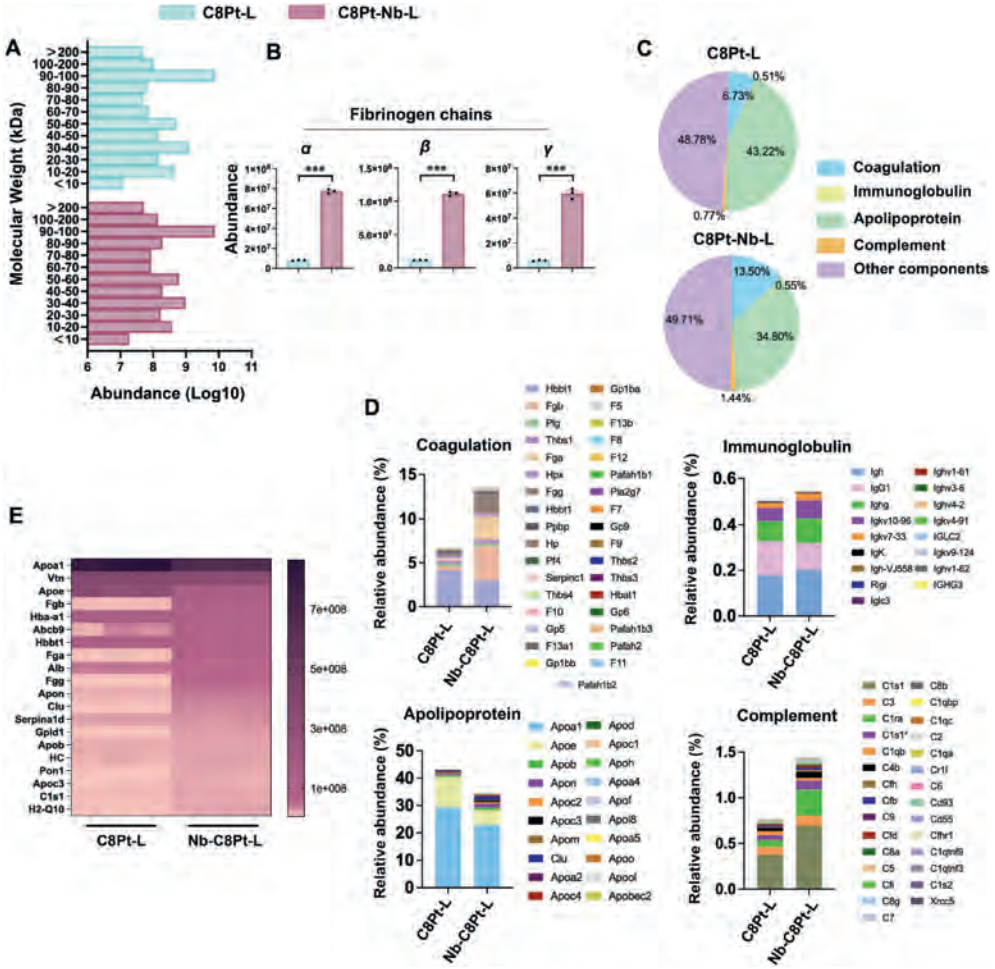

Figure 3 Proteomic comparison of protein coronas absorbed by C8Pt-Ls and Nb-C8Pt-Ls in plasma. (A) Comparison of absorbing proteins coronas based on molecular weight. (B−E) HPLC−MS analysis of the protein coronas absorbed abundance. (B) Absorbed abundance of fibrinogen α, β, and γ chains. (C) The proportion of absorbed protein coronas in distinct biological functions. (D) Absorbed protein coronas in every biological function. (E) The fingerprint of the top 20 most abundant corona proteins absorbed by Nb-C8Pt-Ls. Data are presented as mean ± SEM, $n = 3$, with statistical significance indicated by $^{***}P < 0.001$.

90−100 kD segment exhibiting the highest abundance and the <10 kD segment exhibiting the lowest (Fig. 3A). Abundance analysis indicated a significant, approximately tenfold increase in fibrinogen α, β, and γ chains after anti-fibrinogen Nb decoration (Fig. 3B). Further comparative analysis of the biological functions associated with proteins within the C8Pt-Ls and Nb-C8Pt-Ls coronas revealed shifts in the proportional representation of functional categories. Specifically, the proportion of proteins associated with coagulation increased from 6.73% to 13.50%, immunoglobulin increased from 0.51% to 0.55%, apolipoprotein decreased from 43.22% to 34.80%, and complement increased from 0.77% to 1.44%. Furthermore, the specific proteins within each category also exhibited compositional changes (Fig. 3C and D). In addition, alterations were observed in the top 20 most abundant corona proteins. While the top three proteins (ApoA1, Vtn, and ApoE) remained consistent in rank, their relative abundance decreased after anti-fibrinogen Nb decoration. Notably, the content rankings of Fga, Fgb, and Fgg improved (Fig. 3E and Supporting Information Fig. S4). In contrast, analysis of protein corona composition based on isoelectric points revealed no significant differences (Supporting Information Fig. S5). These findings suggest that anti-fibrinogen Nb decoration modified the protein corona composition of C8Pt-Ls, potentially influencing their targeting efficiency.

3.3. Anti-fibrinogen Nbs facilitated fibrinogen adsorption and LRP-1 binding

The LRP-1 is highly expressed in both the BBB and glioma cells[48]. To explore the interactions between anti-fibrinogen Nbs and fibrinogen, as well as the potential binding of the Nb-fibrinogen complex with LRP-1, molecular docking simulations were conducted. The structures of the three components are shown in Supporting Information Fig. S2. As depicted in Fig. 4A, the binding sites between the anti-fibrinogen Nb and fibrinogen, as well as those between the Nb-fibrinogen complex and LRP-1, were identified. Docking scores and confidence levels indicated stable interactions between the anti-fibrinogen Nbs and fibrinogen, as well as between the Nb-fibrinogen complex and LRP-1 (Fig. 4B). Interaction analysis revealed the formation of hydrogen bonds, electrostatic interactions, and hydrophobic interactions between the anti-fibrinogen Nbs and fibrinogen (Fig. 4C and Supporting Information Table S1). Similarly, hydrogen bonds, salt bridges, and electrostatic and hydrophobic interactions were formed

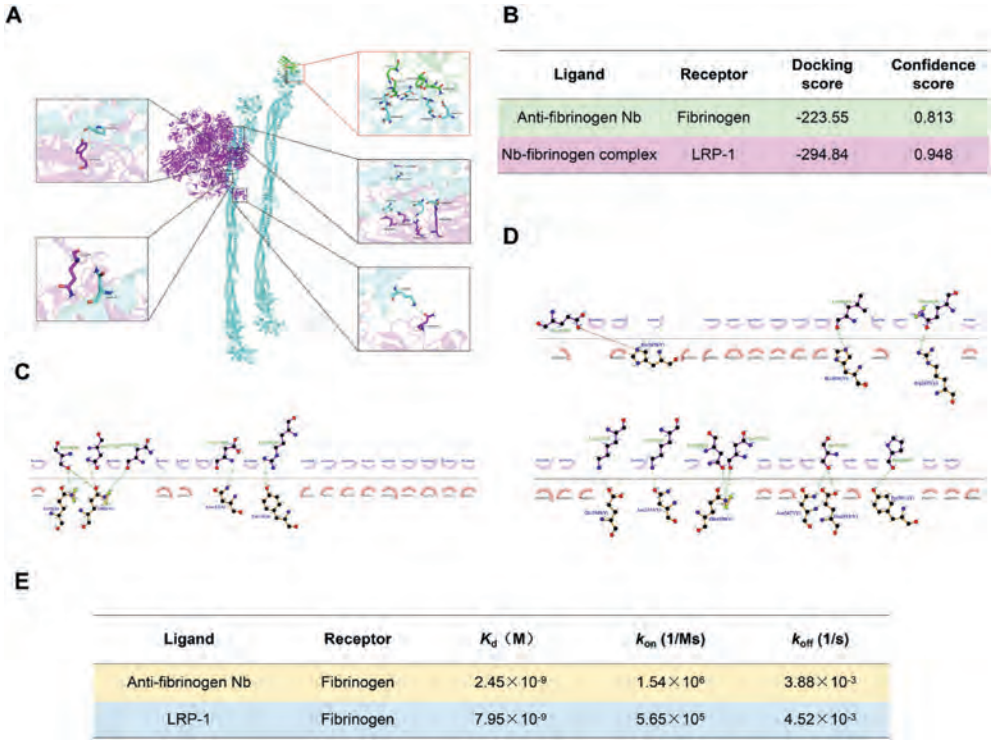

Ligand	Receptor	Docking score	Confidence score
Anti-fibrinogen Nb	Fibrinogen	-223.55	0.813
Nb-fibrinogen complex	LRP-1	-294.84	0.948

Ligand	Receptor	K_d (M)	k_{on} (1/Ms)	k_{off} (1/s)
Anti-fibrinogen Nb	Fibrinogen	2.45×10^{-9}	1.54×10^{6}	3.88×10^{-3}
LRP-1	Fibrinogen	7.95×10^{-9}	5.65×10^{5}	4.52×10^{-3}

Figure 4 Molecular docking of anti-fibrinogen Nb, fibrinogen, and LRP-1 using computer simulation. (A) Molecular docking of anti-fibrinogen Nb (Green), fibrinogen (cyan), and LRP-1 (magenta) complex. Red dash lines marked the binding site between anti-fibrinogen Nb and fibrinogen, and black dash lines marked the four binding sites between Nb-fibrinogen complex and fibrinogen. (B) Molecular docking results of Docking Scores and Confidence Scores. The docking score is calculated by HDock's knowledge-based scoring function. A more negative Docking Score means a higher likelihood of combining models. And confidence score is defined based on experience, which depends on the docking score, to indicate the probability of binding between two molecules. In simple terms, when the Confidence Score is above 0.7, two molecules are likely to combine. (C) Interaction between Anti-fibrinogen Nb and fibrinogen. (D) Interaction between fibrinogen and LRP-1. The green dashed line represented hydrogen bonding interactions, and the red dashed line represented salt bridging interactions. (E) SPR experiments used Biacore to determine interaction affinity of Anti-fibrinogen Nb with fibrinogen, and LRP-1 with fibrinogen. The determination was carried out by coupling proteins with CM5 chips. Dissociation constant (K_d) reflects the affinity of the analyte to the target, with smaller values indicating stronger affinity. Association rate constant (k_{on}) represents the speed of intermolecular binding, with larger values indicating faster binding. Dissociation rate constant (k_{off}) represents the speed of intermolecular dissociation, with larger values indicating faster dissociation.

between the Nb-fibrinogen complex and LRP-1 (Fig. 4D and Supporting Information Table S2). To further demonstrate the efficacy of the hitchhiking strategy, surface plasmon resonance (SPR) was used to determine the binding affinity (K_d value) between fibrinogen and Nb, as well as the interaction between fibrinogen and LRP-1. The K_d values for both interactions were approximately 10^{-9} mol/L, indicating strong binding affinities consistent with the docking scores (Fig. 4E and Supporting Information Fig. S6). The quantity of fibrinogen adsorbed by Nb-C8Pt-Ls increased over time, reaching saturation after approximately 180 min. In contrast, the maximum fibrinogen adsorption on C8Pt-Ls was approximately one-tenth of that observed on Nb-C8Pt-Ls (Supporting Information Fig. S7). These findings suggest that anti-fibrinogen Nbs may promote the adsorption of fibrinogen onto C8Pt-Ls, enabling the nanoparticles to bind to LRP-1 on the BBB. As a result, this mechanism could allow C8Pt-Ls to "hitchhike" on fibrinogen, facilitating their passage across the BBB and enhancing their targeting of brain and glioma tissues.

3.4. *Nb-C8Pt-Ls altered the organ distribution of CisPt*

After evaluating the brain-targeting efficacy of Nb-C8Pt-Ls, we further assessed the brain tumor infiltration and organ distribution of Pt delivered by CisPt, C8Pt-Ls, and Nb-C8Pt-Ls in both *in vitro* and *in vivo* models. In a Transwell assay, after co-incubated the preparations with mouse plasma, Nb-C8Pt-Ls demonstrated superior penetration across bEnd.3 cells, a model of the BBB, compared to both C8Pt-Ls and CisPt (Fig. 5A). The formulation retained nearly the same level of fibrinogen protein corona on its surface after penetrating the bEnd.3 cell layer (Supporting Information Fig. S8). Concurrently, the role of the LRP-1 receptor in Nb-C8Pt-Ls penetration across the BBB was validated. Pre-treatment of bEnd.3 cells with Atorvastatin (an LRP-1 inhibitor) resulted in a significant decrease in Nb-C8Pt-Ls penetration, reaching a level comparable to that of C8Pt-Ls penetrating the BBB. This finding indicates the crucial role of the LRP-1 receptor in this "Hitchhiking Effect" (Supporting Information Fig. S9). Additionally, Nb-C8Pt-Ls exhibited the highest uptake into both bEnd.3 cells and GL261-LUC glioma cells among the three formulations (Fig. 5B).

In vivo experiments further validated these findings, confirming that Nb-C8Pt-Ls exhibited the most effective brain and tumor targeting, achieving approximately two-fold and three-fold higher accumulation, respectively, compared to C8Pt-Ls (Fig. 5C). We then evaluated the organ distribution of Pt at various time points after intravenous injection, focusing on the heart, liver, spleen, lungs, and kidneys. In the C8Pt-L group, higher Pt accumulation was observed in the heart, liver, spleen, and lungs, with the exception of the kidney, when compared to the CisPt group. Additionally, Pt remained in the bloodstream longer in the C8Pt-L group. In contrast, the Nb-C8Pt-L group showed increased Pt retention in the heart and bloodstream, with reduced levels in the liver, spleen, lungs, and kidneys (Fig. 5D). These findings indicate that Nb-C8Pt-Ls achieved dual targeting of both the brain and

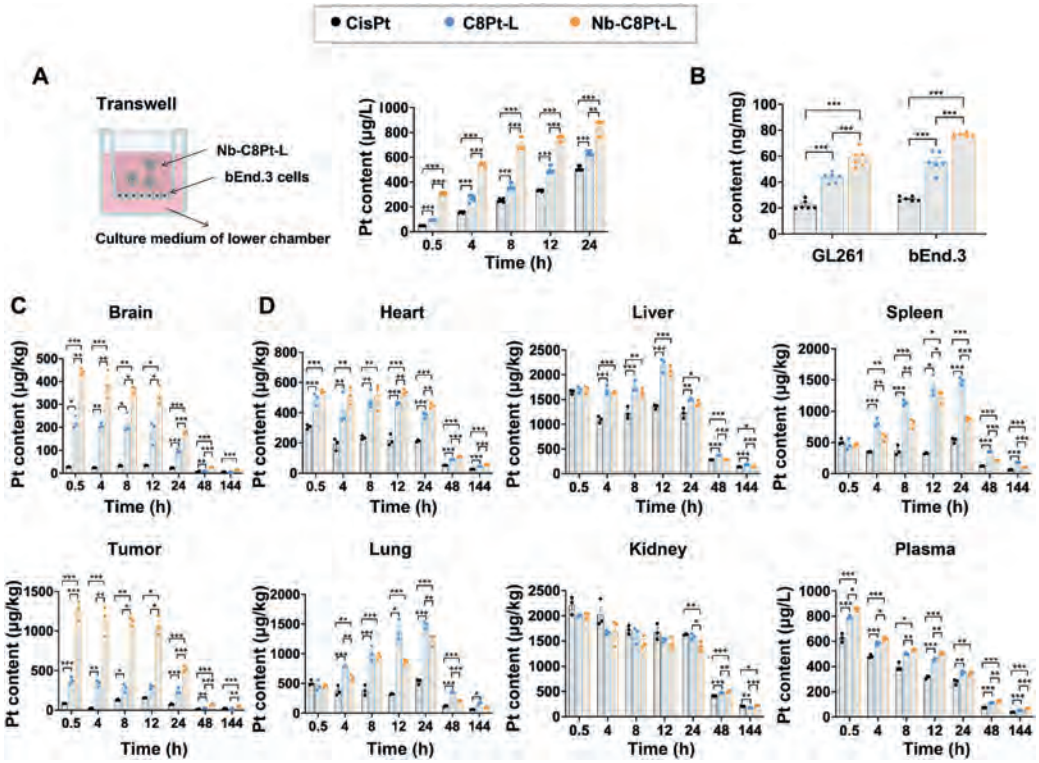

Figure 5 Brain and tumor targeting efficiency of Nb-C8Pt-Ls *in vitro* and *in vivo*. (A) A Transwell assay was performed to determine the Pt concentration in the lower chamber's culture medium at different time points using ICP-MS. (B) Pt accumulation was quantified in GL261 and bEnd.3 cells after a 6-h treatment with the respective preparations. (C) Pt levels were measured in the brain and tumor tissues of treated mice at various time points. (D) Pt concentrations were also analyzed in the heart, liver, spleen, lung, kidneys, and plasma of treated mice over time. Data are reported as mean ± SEM, with $n = 3$. Statistical significance is denoted as $^{*}P < 0.05$, $^{**}P < 0.01$, and $^{***}P < 0.001$. CisPt referred to cisplatin, C8Pt-L to C8Pt LNP, and Nb-C8Pt-L to Anti-fibrinogen Nb-modified C8Pt LNP.

tumors, outperforming CisPt and C8Pt-Ls in both *in vitro* and *in vivo* studies. The enhanced targeting capabilities were coupled with reduced Pt distribution to several major organs, suggesting improved specificity and the potential for reduced systemic toxicity, thus offering a promising approach for safer and more effective glioma treatments.

3.5. *Nb-C8Pt-Ls enhanced anti-glioma activity*

Following confirmation of the brain and tumor-targeting capabilities of Nb-C8Pt-Ls *in vitro* and *in vivo*, their anti-glioma efficacy was evaluated using a glioma-bearing mouse model. After establishing the model and administering intravenous treatments, Nb-

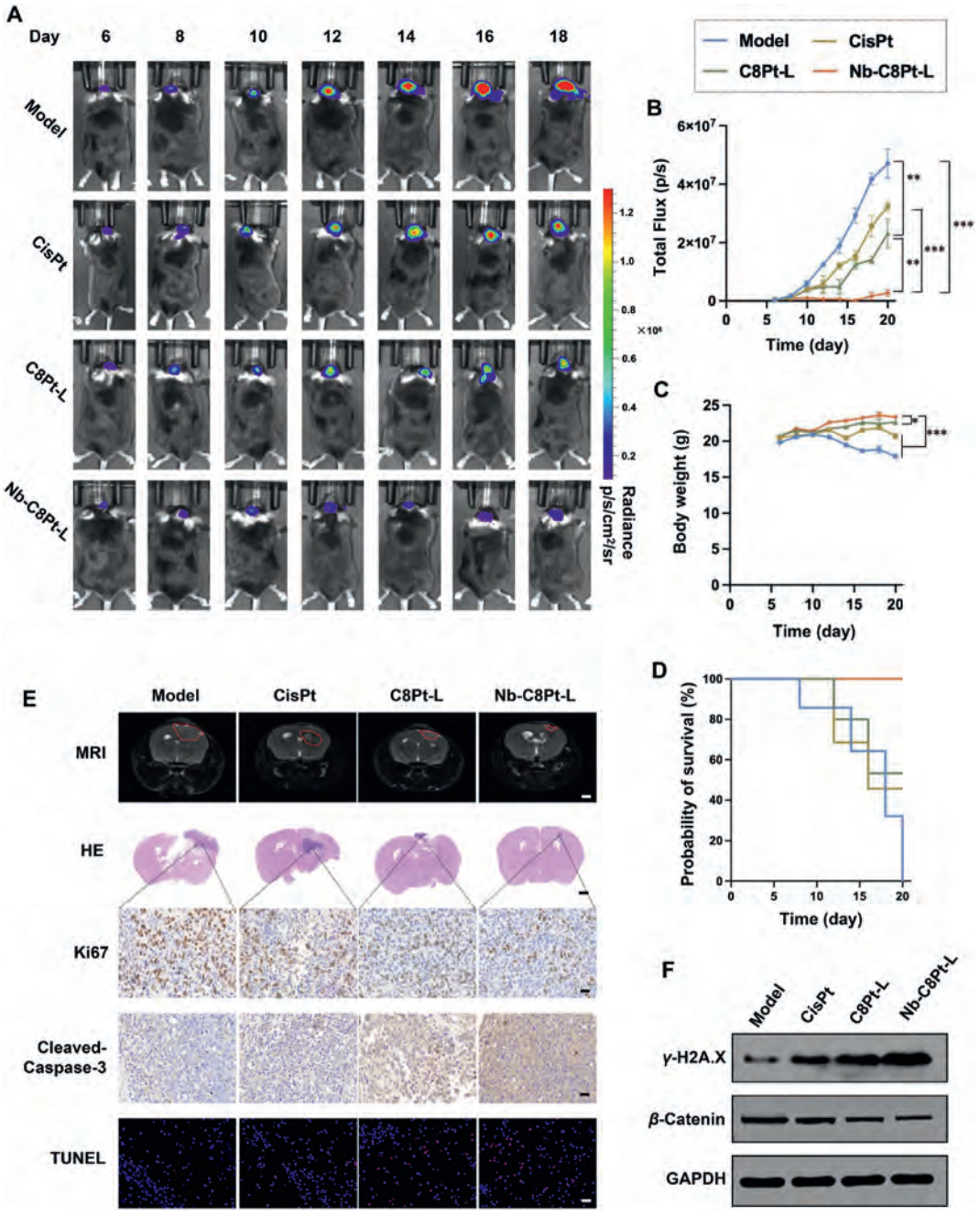

Figure 6 *In vivo* anti-glioma efficacy of Nb-C8Pt-Ls. (A, B) Representative bioluminescence images and corresponding quantitative analysis of GL261-LUC glioma-bearing mice were conducted across various treatment groups, with formulations administered every two days. (C, D) Body weight and survival rates of tumor-bearing mice were monitored throughout the study period. (E) At the end of the experiment, MRI T2 images were acquired, and histological analyses, including H&E staining (scale bar = 1 mm), Ki67 IHC staining, cleaved caspase-3 IHC staining, and TUNEL staining (scale bar = 20 μm), were conducted on brain tissues. (F) Western blot analysis was used to assess the expression of γ-H2A.X and β-catenin in tumor tissues. Data are presented as mean ± SEM, with $n = 6$. Statistical significance was indicated as $^{*}P < 0.05$, $^{**}P < 0.01$, and $^{***}P < 0.001$. CisPt refers to cisplatin, C8Pt-L to C8Pt LNP, and Nb-C8Pt-L to anti-fibrinogen Nb-modified C8Pt LNP.

C8Pt-Ls exhibited superior inhibition of glioma growth compared to C8Pt-Ls and CisPt, with the most pronounced tumor suppression observed in the Nb-C8Pt-Ls group (Fig. 6A and B). In addition, Nb-C8Pt-Ls effectively prevented the body weight loss typically associated with glioma progression, whereas C8Pt-Ls and CisPt demonstrated progressively less effectiveness in mitigating this side effect (Fig. 6C). Survival probability followed a similar trend, with the Nb-C8Pt-Ls-treated group exhibiting the highest survival rate, reaching 100% (Fig. 6D). Magnetic resonance imaging (MRI) and hematoxylin and eosin (HE) staining confirmed that the Nb-C8Pt-Ls-treated mice had the smallest glioma volumes at the conclusion of the experiment compared to those treated with C8Pt-Ls or CisPt (Fig. 6E). Several biomarkers were analyzed to further assess the therapeutic efficacy of Nb-C8Pt-Ls (Fig. 6E and F). γ-H2A.X, a marker of DNA double-strand breaks, was significantly expressed in the Nb-C8Pt-L-treated group. Terminal deoxynucleotidyl transferase (TdT) dUTP nick end labeling (TUNEL) staining also revealed a higher degree of DNA fragmentation in this group. Furthermore, cleaved caspase-3, a key enzyme in the apoptosis pathway, was more highly expressed in glioma tissues treated with Nb-C8Pt-Ls. Conversely, β-catenin and Ki67, which are associated with tumor proliferation, infiltration, and metastasis, were expressed at lower levels in the Nb-C8Pt-L group compared to the other treatment groups. These results indicate that Nb-C8Pt-Ls more effectively delivered CisPt to brain tumor tissues, leading to enhanced DNA damage and increased apoptosis in glioma cells. The findings suggest that Nb-C8Pt-Ls hold significant promise as a potent anti-glioma therapy, offering a more effective strategy by promoting DNA breakage and apoptosis in tumor cells.

3.6. *Nb-C8Pt-Ls exhibited ideal safety*

Beyond efficacy, the biosafety of Nb-C8Pt-Ls was thoroughly evaluated, as safety is a critical consideration for the clinical application of nanomedicine. Pathological examinations of major

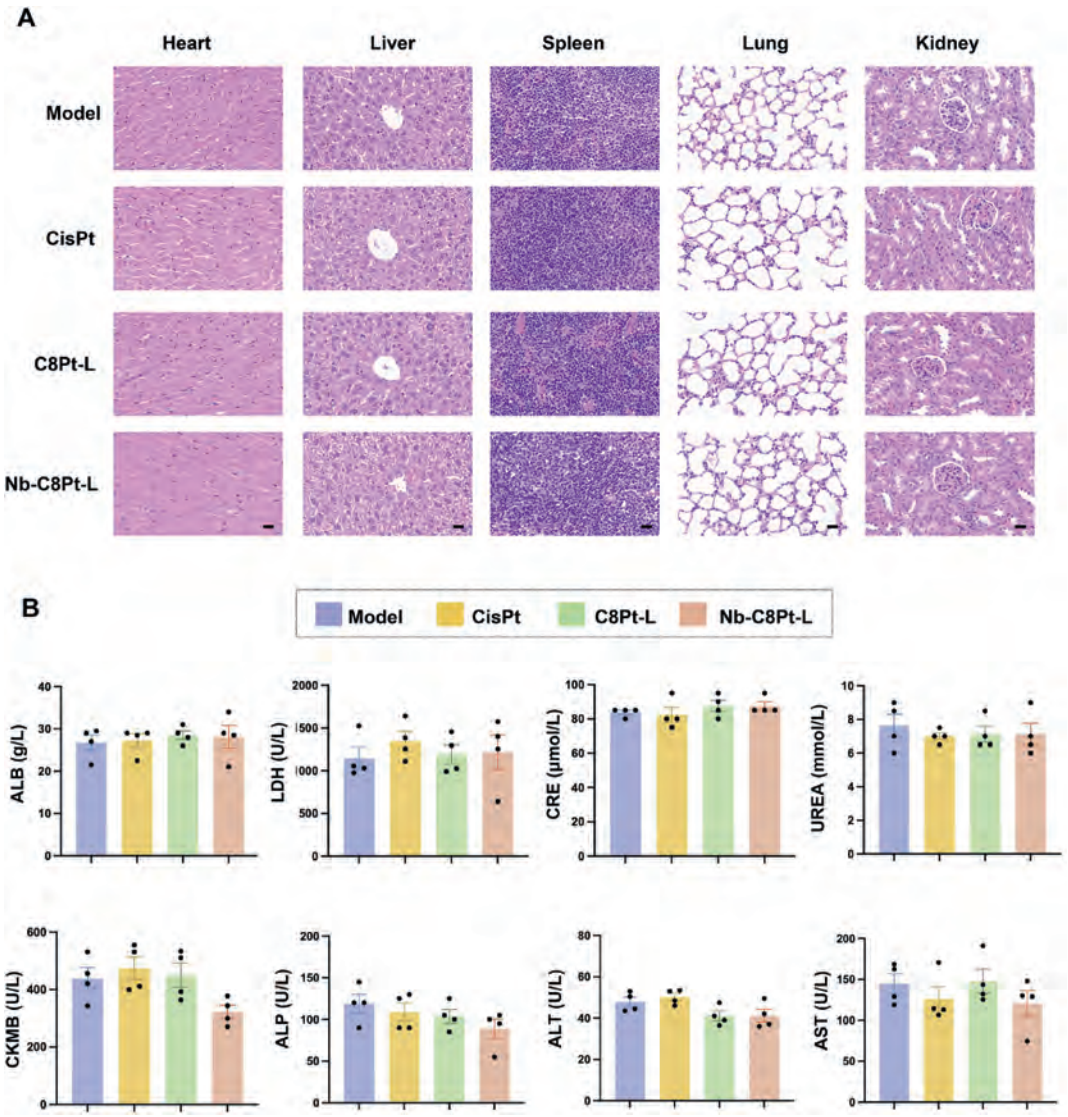

Figure 7 *In vivo* safety evaluation of CisPt, C8Pt-Ls, and Nb-C8Pt-Ls. (A) H&E staining was conducted on major organs (scale bar = 20 μm) to evaluate potential toxicity. (B) Blood biochemistry analyses were performed in groups treated with CisPt, C8Pt-Ls, and Nb-C8Pt-Ls. Data are depicted as the mean (black solid line) ± quartiles (white dotted lines) in violin plots, with $n = 4$. CisPt referred to cisplatin, C8Pt-L to C8Pt LNP, and Nb-C8Pt-L to Anti-fibrinogen Nb-modified C8Pt LNP.

organs, including the heart, liver, spleen, lungs, and kidneys, revealed no significant abnormalities or safety concerns across all treatment groups (Fig. 7A). The modification with anti-fibrinogen Nbs did not elevate anti-Nb antibody levels in the serum (Supporting Information Fig. S10), possibly due to the low immunogenicity of Nb's intrinsic characteristic. Furthermore, the modification with anti-fibrinogen Nbs did not affect coagulation function, as the prothrombin time (PT) remained within the range of 11−15 s (Supporting Information Fig. S11).

Additionally, blood biochemical tests were performed to assess potential organ toxicity, focusing on key markers such as albumin (ALB), lactate dehydrogenase (LDH), creatinine (CRE), urea (UREA), creatine kinase-MB (CKMB), alkaline phosphatase (ALP), alanine aminotransferase (ALT), and aspartate aminotransferase (AST). The results showed no significant differences in these markers between groups, indicating that Nb-C8Pt-Ls did not induce liver, kidney, or cardiac toxicity (Fig. 7B). In conclusion, Nb-C8Pt-Ls demonstrated an excellent safety profile, with no observable organ damage or significant biochemical changes. These findings suggest that Nb-C8Pt-Ls are both effective and safe, supporting their potential for clinical use in glioma treatment.

4. Discussion

The BBB remains a significant obstacle to the clinical application of CisPt for brain tumor treatment. In this study, a hydrophobically modified form of CisPt, C8Pt, was synthesized and encapsulated into LNPs. These LNPs were further modified with Nbs to create Nb-C8Pt-Ls, which demonstrated favorable characterization properties. C8Pt-Ls stained with lipophilic dye effectively targeted both brain and tumor tissues. The Nb modification on the liposomes altered the protein corona formation in plasma, notably increasing the adsorption of fibrinogen. Through computer simulations and SRP detection, we identified the binding mode and sites for the Nb-fibrinogen-(LRP-1) interaction. *In vivo*, Nb-C8Pt-Ls exhibited reduced distribution in other organs while increasing brain and tumor targeting *via* the "Hitchhiking Effect". This delivery system effectively induced apoptosis in brain tumor tissues in glioma-bearing mouse models while maintaining a favorable safety profile. These results indicate that Nb-C8Pt-Ls hold great potential for safe and effective glioma treatment.

Currently, despite the promising progress of various strategies for intracranial drug delivery, clinical translation remains limited. Approaches include intracranial injection, nasal administration, temporary disruption of the BBB, cell-penetrating peptides, and receptor-mediated BBB penetration[31]. For instance, while intracranial injection offers direct drug delivery, it is an invasive procedure associated with high risks, such as brain infection, edema, and solution reflux, which limit its clinical feasibility[1]. Nasal administration is a non-invasive alternative, bypassing systemic circulation to deliver drugs to the brain. However, the limited surface area of the olfactory region, which comprises only about 5% of the human nasal epithelium, restricts both drug dosage and bioavailability[49]. Temporary disruption of the BBB is another common method to enhance drug permeability in the brain, but it can inadvertently allow toxic substances to enter the central nervous system, compromising normal function[50]. In summary, while these methods provide different routes for overcoming the BBB, their limitations highlight the need for safer and more efficient strategies, such as Nb-C8Pt-Ls, which can provide targeted delivery without invasive procedures or significant risk of systemic toxicity.

In our design, LNPs were modified with Nbs possessing low immunogenicity[28] (Supporting Information Fig. S10). These modified LNPs preferentially adsorbed fibrinogen coronas from plasma, enabling them to penetrate the BBB *via* a "Hitchhiking Effect", providing a gentle and minimally invasive approach. We observed that anti-Fibrinogen Nb modification on LNPs was stable (Fig. 2I and J), and the rate of fibrinogen adsorption in plasma was also rapid and consistent (Fig. S7). Furthermore, the modified LNPs maintained high structural integrity after penetrating the BBB (Fig. S8), which facilitated their subsequent targeting of glioma cells. Previous studies have explored Pt-based drug-loaded nano-carriers or chemically decorated Pt-based drug for brain delivery[51-54], whereas these vectors might be criticized for their rapid renal clearance and uncontrolled drug release. Importantly, our delivery system, which mimics the structure of mRNA LNPs, may offer superior biocompatibility with the human body[55]. Notably, C8Pt-Ls demonstrated enhanced brain and tumor-targeting effects compared to CisPt (Fig. 5C and D), likely due to the hydrophobic nature of the LNP nanocarrier, which might be more superior than other polymeric nanoparticles[56] and easier to modify target head to the surface of the particle. Furthermore, at high-glutathione (GSH) tumor sites, C8Pt-Ls take advantage of the reduction of Pt^{4+} to Pt^{2+}, enhancing their pharmacodynamic activity.

Our research also investigated the specific mechanisms through which the nanocarriers cross the BBB. One significant challenge for the clinical translation of targeted drug delivery systems is protein corona formation, which can reduce targeting efficiency and cause undesirable biodistribution. However, corona-mediated targeting introduces a novel approach by carefully controlling interactions between functional plasma proteins and the nanoparticle surface[30]. In this study, we repurposed the traditionally perceived disadvantages of protein coronas, leveraging the "Hitchhiking Effect" of these coronas for dual targeting of the brain and tumor. Various properties of protein coronas, such as isoelectric point, molecular weight, and biological functions, are known to influence organ-targeting characteristics[57,58]. Consistent with the observed increase in brain targeting of LNPs following modification with anti-fibrinogen Nbs, our results revealed alterations in the properties of the adsorbed protein coronas, notably an increase in fibrinogen, along with changes in other components (Fig. 3, Figs. S4 and S5). Future research should focus on further elucidating the functional relationship between the increased abundance of these other components and brain targeting efficiency. In this study, we repurposed the traditionally perceived disadvantages of protein coronas, leveraging the "Hitchhiking Effect" of these coronas for dual targeting of the brain and tumor. Additionally, we noted that staining with different dyes resulted in slight variations in brain-targeting efficiency (Fig. 2L−N and Fig. S3), which may be due to the dyes altering the characteristics of the protein coronas. Further studies are needed to explore these interactions, which could lead to refined nanoparticle-based drug delivery systems with improved precision.

Surprisingly, no hepatorenal toxicity was observed *in vivo* with the administration of CisPt solution (Fig. 7). However, it is well-established that increasing the dosage and frequency of Pt-based drugs can lead to toxic effects due to their accumulation in the liver and kidneys[8]. In contrast, the use of C8Pt-Ls and Nb-C8Pt-Ls significantly alters the distribution of the drug across various organs and modifies its pharmacokinetic properties, which helps reduce the potential for toxicity. This redistribution, coupled with the targeted delivery mechanism provided by Nb-C8Pt-Ls, contributes to minimizing the systemic toxicity commonly associated with Pt-based chemotherapy. The modification with anti-fibrinogen Nbs did not affect plasma prothrombin time (PT)

(Fig. S11). Consistent with our earlier observation of a slight increase in coagulation within the plasma protein coronas adsorbed by C8Pt-Ls and Nb-C8Pt-Ls (Fig. 3D), these findings suggest that our formulation does not compromise plasma coagulation function. These improvements suggest that such formulations may offer a safer alternative for clinical applications, enhancing treatment efficacy while lowering the risk of adverse side effects.

5. Conclusions

This research introduced a pioneering approach by decorating the surface of C8Pt-Ls with anti-fibrinogen Nbs to modulate protein corona formation. By utilizing the "Hitchhiking Effect" in which Nb-C8Pt-Ls absorbed fibrinogen from plasma, this system enabled efficient penetration of the BBB and targeted glioma tissues specifically. This innovative strategy not only improves the delivery efficiency of Pt-based drugs but also enhances their therapeutic impact, leading to significantly improved anti-glioma efficacy.

Acknowledgments

The work was supported by the National Natural Science Foundation of China (22107080 and 82300113).

Author contributions

Conceptualization: Hai Huang and Xiangrong Song. Methodology and investigation: Yupei Zhang, Shugang Qin, Tingting Song, Zhiying Huang, Zekai Lv, Yang Zhao, Xiangyu Jiao, Min Sun, Yinghan Zhang, Guang Xie, Yuting Chen, Xuli Ruan, Ruyue Liu, Haixing Shi, Chunli Yang, and Siyu Zhao. Visualization: Hai Huang and Xiangrong Song. Supervision: Hai Huang, Xiangrong Song, and Zhongshan He. Writing original draft: Yupei Zhang, and Shugang Qin. Writing−review & editing: Yupei Zhang, Shugang Qin, Tingting Song, Hai Huang, and Xiangrong Song. All of the authors have read and approved the final manuscript.

Conflicts of interest

The authors have no conflicts of interest to declare.

Appendix A. Supporting information

Supporting information to this article can be found online at https://doi.org/10.1016/j.apsb.2025.07.014.

References

1. Allhenn D, Boushehri MA, Lamprecht A. Drug delivery strategies for the treatment of malignant gliomas. *Int J Pharm* 2012;**436**: 299−310.
2. Lipkova J, Menze B, Wiestler B, Koumoutsakos P, Lowengrub JS. Modelling glioma progression, mass effect and intracranial pressure in patient anatomy. *J R Soc Interface* 2022;**19**:20210922.
3. Weller M, Wen PY, Chang SM, Dirven L, Lim M, Monje M, et al. Glioma. *Nat Rev Dis Primers* 2024;**10**:33.
4. Oronsky B, Reid TR, Oronsky A, Sandhu N, Knox SJ. A review of newly diagnosed glioblastoma. *Front Oncol* 2020;**10**:574012.
5. Daniel P, Sabri S, Chaddad A, Meehan B, Jean-Claude B, Rak J, et al. Temozolomide induced hypermutation in glioma: evolutionary mechanisms and therapeutic opportunities. *Front Oncol* 2019;**9**:41.
6. Poon WS, Woo PM, Li Y, Chan AY, Ng SP, Loong HF, et al. A multifaceted review of temozolomide resistance mechanisms in glioblastoma beyond *O*-6-methylguanine-DNA methyltransferase. *Glioma* 2019;**2**:68−82.
7. Li T, Li J, Chen Z, Zhang S, Li S, Wageh S, et al. Glioma diagnosis and therapy: current challenges and nanomaterial-based solutions. *J Control Release* 2022;**352**:338−70.
8. Zhang C, Xu C, Gao X, Yao Q. Platinum-based drugs for cancer therapy and anti-tumor strategies. *Theranostics* 2022;**12**: 2115−32.
9. Rottenberg S, Disler C, Perego P. The rediscovery of platinum-based cancer therapy. *Nat Rev Cancer* 2021;**21**:37−50.
10. Jeon J, Lee S, Kim H, Kang H, Youn H, Jo S, et al. Revisiting platinum-based anticancer drugs to overcome gliomas. *Int J Mol Sci* 2021;**22**:5111.
11. Roci E, Cakani B, Brace G, Bushati T, Rroji A, Petrela M, et al. Platinum-based chemotherapy in recurrent high-grade glioma patients: retrospective study. *Med Arch* 2014;**68**:140−3.
12. Dhar S, Kolishetti N, Lippard SJ, Farokhzad OC. Targeted delivery of a cisplatin prodrug for safer and more effective prostate cancer therapy *in vivo*. *Proc Natl Acad Sci U S A* 2011;**108**:1850−5.
13. Zhang S, Jiang W, Wang S, Song K, Ge M, Zhang L, et al. Cancer cell membrane fused liposomal platinum(IV) prodrugs overcome cisplatin resistance in esophageal squamous cell carcinoma chemotherapy. *J Mater Chem B* 2023;**11**:11384−93.
14. Poon C, Duan X, Chan C, Han W, Lin W. Nanoscale coordination polymers codeliver carboplatin and gemcitabine for highly effective treatment of platinum-resistant ovarian cancer. *Mol Pharm* 2016;**13**: 3665−75.
15. Xiao H, Song H, Yang Q, Cai H, Qi R, Yan L, et al. A prodrug strategy to deliver cisplatin(IV) and paclitaxel in nanomicelles to improve efficacy and tolerance. *Biomaterials* 2012;**33**:6507−19.
16. Chang C, Wang C, Zhang C, Li L, Zhang Q, Huang Q. Albumin-encapsulated platinum nanoparticles for targeted photothermal treatment of glioma. *J Biomed Nanotechnol* 2019;**15**:1744−53.
17. Johnstone TC, Suntharalingam K, Lippard SJ. The next generation of platinum drugs: targeted Pt(II) agents, nanoparticle delivery, and Pt (IV) prodrugs. *Chem Rev* 2016;**116**:3436−86.
18. Xu L, Kong X, Li X, Zhang B, Deng Y, Wang J, et al. Current status of novel multifunctional targeted Pt(IV) compounds and their reductive release properties. *Molecules* 2024;**29**:746.
19. Fang G, Zhang A, Zhu L, Wang Q, Sun F, Tang B. Nanocarriers containing platinum compounds for combination chemotherapy. *Front Pharmacol* 2022;**13**:1050928.
20. Alphandery E. Nano-therapies for glioblastoma treatment. *Cancers (Basel)* 2020;**12**:242.
21. Cai R, Chen C. The crown and the scepter: roles of the protein corona in nanomedicine. *Adv Mater* 2019;**31**:e1805740.
22. Hu M, Li X, You Z, Cai R, Chen C. Physiological barriers and strategies of lipid-based nanoparticles for nucleic acid drug delivery. *Adv Mater* 2024;**36**:e2303266.
23. Amici A, Pozzi D, Marchini C, Caracciolo G. The transformative potential of lipid nanoparticle-protein corona for next-generation vaccines and therapeutics. *Mol Pharm* 2023;**20**:5247−53.
24. Ban Z, Yuan P, Yu F, Peng T, Zhou Q, Hu X. Machine learning predicts the functional composition of the protein corona and the cellular recognition of nanoparticles. *Proc Natl Acad Sci U S A* 2020;**117**: 10492−9.
25. Zhao Z, Ukidve A, Kim J, Mitragotri S. Targeting strategies for tissue-specific drug delivery. *Cell* 2020;**181**:151−67.
26. Buss NA, Henderson SJ, McFarlane M, Shenton JM, de Haan L. Monoclonal antibody therapeutics: history and future. *Curr Opin Pharmacol* 2012;**12**:615−22.
27. Nanobodies Muyldermans S. Natural single-domain antibodies. *Annu Rev Biochem* 2013;**82**:775−97.
28. Sun S, Ding Z, Yang X, Zhao X, Zhao M, Gao L, et al. Nanobody: a small antibody with big implications for tumor therapeutic strategy. *Int J Nanomed* 2021;**16**:2337−56.

29. Zhang ZA, Xin X, Liu C, Liu YH, Duan HX, Qi LL, et al. Novel brain-targeted nanomicelles for anti-glioma therapy mediated by the ApoE-enriched protein corona *in vivo*. *J Nanobiotechnol* 2021;**19**:453.
30. Zhang Z, Guan J, Jiang Z, Yang Y, Liu J, Hua W, et al. Brain-targeted drug delivery by manipulating protein corona functions. *Nat Commun* 2019;**10**:3561.
31. Xie J, Shen Z, Anraku Y, Kataoka K, Chen X. Nanomaterial-based blood-brain-barrier (BBB) crossing strategies. *Biomaterials* 2019; **224**:119491.
32. Chen S, Li L, Peng C, Bian C, Ocak PE, Zhang JH, et al. Targeting oxidative stress and inflammatory response for blood-brain barrier protection in intracerebral hemorrhage. *Antioxid Redox Signal* 2022;**37**: 115−34.
33. Petersen MA, Ryu JK, Akassoglou K. Fibrinogen in neurological diseases: mechanisms, imaging and therapeutics. *Nat Rev Neurosci* 2018;**19**:283−301.
34. Alruwaili M, Al-Kuraishy HM, Alexiou A, Papadakis M, Bm AL, Elhussieny O, et al. Pathogenic role of fibrinogen in the neuropathology of multiple sclerosis: a tale of sorrows and fears. *Neurochem Res* 2023;**48**:3255−69.
35. Salema V, Lopez-Guajardo A, Gutierrez C, Mencia M, Fernandez LA. Characterization of nanobodies binding human fibrinogen selected by *E. coli* display. *J Biotechnol* 2016;**234**:58−65.
36. Abramson J, Adler J, Dunger J, Evans R, Green T, Pritzel A, et al. Accurate structure prediction of biomolecular interactions with AlphaFold 3. *Nature* 2024;**630**:493−500.
37. Berman HM, Westbrook J, Feng Z, Gilliland G, Bhat TN, Weissig H, et al. The protein data bank. *Nucleic Acids Res* 2000;**28**: 235−42.
38. Yan Y, Tao H, He J, Huang SY. The HDOCK server for integrated protein−protein docking. *Nat Protoc* 2020;**15**:1829−52.
39. Yan Y, Zhang D, Zhou P, Li B, Huang SY. HDOCK: a web server for protein−protein and protein-DNA/RNA docking based on a hybrid strategy. *Nucleic Acids Res* 2017;**45**:W365−73.
40. Yan Y, Wen Z, Wang X, Huang SY. Addressing recent docking challenges: a hybrid strategy to integrate template-based and free protein−protein docking. *Proteins* 2017;**85**:497−512.
41. Huang SY, Zou X. A knowledge-based scoring function for protein-RNA interactions derived from a statistical mechanics-based iterative method. *Nucleic Acids Res* 2014;**42**:e55.
42. Huang SY, Zou X. An iterative knowledge-based scoring function for protein−protein recognition. *Proteins* 2008;**72**:557−79.
43. Monopoli MP, Walczyk D, Campbell A, Elia G, Lynch I, Bombelli FB, et al. Physical-chemical aspects of protein corona: relevance to *in vitro* and *in vivo* biological impacts of nanoparticles. *J Am Chem Soc* 2011;**133**:2525−34.
44. Qiu M, Tang Y, Chen J, Muriph R, Ye Z, Huang C, et al. Lung-selective mRNA delivery of synthetic lipid nanoparticles for the treatment of pulmonary lymphangioleiomyomatosis. *Proc Natl Acad Sci U S A* 2022;**119**:e2116271119.
45. Wang Y, Huo Y, Zhao C, Liu H, Shao Y, Zhu C, et al. Engineered exosomes with enhanced stability and delivery efficiency for glioblastoma therapy. *J Control Release* 2024;**368**:170−83.
46. Tang L, Zhang R, Wang Y, Liu M, Hu D, Wang Y, et al. A blood-brain barrier- and blood-brain tumor barrier-penetrating siRNA delivery system targeting gliomas for brain tumor immunotherapy. *J Control Release* 2024;**369**:642−57.
47. Zhang YP, Yang XQ, Yu DK, Xiao HY, Du JR. Nrf2 signalling pathway and autophagy impact on the preventive effect of green tea extract against alcohol-induced liver injury. *J Pharm Pharmacol* 2021;**73**:986−95.
48. Gao DL, Johal MS. LRP-1 binds fibrinogen in a sialylation-dependent manner: a quartz crystal microbalance study. *Langmuir* 2023;**39**: 10375−82.
49. Kozlovskaya L, Abou-Kaoud M, Stepensky D. Quantitative analysis of drug delivery to the brain *via* nasal route. *J Control Release* 2014; **189**:133−40.
50. Kozler P, Pokorny J. Effect of methylprednisolone on the axonal impairment accompanying cellular brain oedema induced by water intoxication in rats. *Neuroendocrinol Lett* 2012;**33**: 782−6.
51. Miura Y, Takenaka T, Toh K, Wu S, Nishihara H, Kano MR, et al. Cyclic RGD-linked polymeric micelles for targeted delivery of platinum anticancer drugs to glioblastoma through the blood−brain tumor barrier. *ACS Nano* 2013;**7**:8583−92.
52. Sun T, Jiang X, Wang Q, Chen Q, Lu Y, Liu L, et al. Substance P mediated DGLs complexing with DACHPt for targeting therapy of glioma. *ACS Appl Mater Interfaces* 2017;**9**:34603−17.
53. Jimenez-Macias JL, Lee YC, Miller E, Finkelberg T, Zdioruk M, Berger G, et al. A Pt(IV)-conjugated brain penetrant macrocyclic peptide shows pre-clinical efficacy in glioblastoma. *J Control Release* 2022;**352**:623−36.
54. Noble GT, Stefanick JF, Ashley JD, Kiziltepe T, Bilgicer B. Ligand-targeted liposome design: challenges and fundamental considerations. *Trends Biotechnol* 2014;**32**:32−45.
55. Zong Y, Lin Y, Wei T, Cheng Q. Lipid nanoparticle (LNP) enables mRNA delivery for cancer therapy. *Adv Mater* 2023;**35**:e2303261.
56. Khare P, Edgecomb SX, Hamadani CM, Tanner EEL, D SM. Lipid nanoparticle-mediated drug delivery to the brain. *Adv Drug Deliv Rev* 2023;**197**:114861.
57. Yang Z, Liu Y, Zhao K, Jing W, Gao L, Dong X, et al. Dual mRNA co-delivery for *in situ* generation of phagocytosis-enhanced CAR macrophages augments hepatocellular carcinoma immunotherapy. *J Control Release* 2023;**360**:718−33.
58. Dilliard SA, Cheng Q, Siegwart DJ. On the mechanism of tissue-specific mRNA delivery by selective organ targeting nanoparticles. *Proc Natl Acad Sci U S A* 2021;**118**:e2109256118.